A unique probe of dark matter in the core of M87 with the Event Horizon Telescope

Thomas Lacroix,[1,2] Mansour Karami,[3,4] Avery E. Broderick,[3,4] Joseph Silk,[1,5,6] and Céline Bœhm[7,8]

[1]*Institut d'Astrophysique de Paris, UMR 7095, CNRS, UPMC Université Paris 6, Sorbonne Universités, 98 bis boulevard Arago, 75014 Paris, France*
[2]*Laboratoire Univers & Particules de Montpellier (LUPM), CNRS & Université de Montpellier (UMR 5299), Place Eugène Bataillon, F-34095 Montpellier Cedex 05, France**
[3]*Perimeter Institute for Theoretical Physics, 31 Caroline Street North, Waterloo, ON N2L 2Y5, Canada*
[4]*Department of Physics and Astronomy, University of Waterloo, 200 University Avenue West, Waterloo, ON N2L 3G1, Canada*
[5]*The Johns Hopkins University, Department of Physics and Astronomy, 3400 N. Charles Street, Baltimore, Maryland 21218, USA*
[6]*Beecroft Institute of Particle Astrophysics and Cosmology, Department of Physics, University of Oxford, Denys Wilkinson Building, 1 Keble Road, Oxford OX1 3RH, United Kingdom*
[7]*Institute for Particle Physics Phenomenology, Durham University, Durham, DH1 3LE, United Kingdom*
[8]*LAPTH, Université de Savoie, CNRS, BP 110, 74941 Annecy-Le-Vieux, France*

(Dated: November 8, 2016)

We demonstrate the unprecedented capabilities of the Event Horizon Telescope (EHT) to image the innermost dark matter profile in the vicinity of the supermassive black hole at the center of the M87 radio galaxy. We present the first model of the synchrotron emission induced by dark matter annihilations from a spiky profile in the close vicinity of a supermassive black hole, accounting for strong gravitational lensing effects. Our results show that the EHT should readily resolve dark matter spikes if present. Moreover, the photon ring surrounding the silhouette of the black hole is clearly visible in the spike emission, which introduces observable small-scale structure into the signal. We find that the dark matter-induced emission provides an adequate fit to the existing EHT data, implying that in addition to the jet, a dark matter spike may account for a sizable portion of the millimeter emission from the innermost (sub-parsec) region of M87. Regardless, our results show that the EHT can probe very weakly annihilating dark matter. Current EHT observations already constrain very small cross-sections, typically down to a few 10^{-31} cm^3 s^{-1} for a 10 GeV candidate, close to characteristic values for p-wave-suppressed annihilation. Future EHT observations will further improve constraints on the DM scenario.

PACS numbers: 95.35.+d, 96.50.S-, 95.55.Br

arXiv:1611.01961v1 [astro-ph.GA] 7 Nov 2016

I. INTRODUCTION

The dark matter (DM) density profile at the centers of galaxies is critical to indirect searches but remains poorly constrained. In objects such as M87, the DM profile may be significantly enhanced on sub-parsec scales by the central supermassive black hole (SMBH), although there is no direct evidence for such a sharp density increase, referred to as a DM spike.

DM spikes however leave a very distinctive signature in the spectral energy distribution (SED) of a galaxy if DM can annihilate [1]. More specifically, in the case of M87, where a spike should plausibly have formed and survived galaxy dynamics, an anomalous contribution to the SED is expected when the DM annihilation cross-section is larger than $\sim 10^{-30}$ cm^3 s^{-1} for light (10 to 100 GeV) DM particles, and above $\sim 3\times10^{-26}$ cm^3 s^{-1} for candidates as heavy as 100 TeV.

Here we show that it is possible to probe even fainter DM-induced radiation in M87 by using the spatial morphology of the DM-induced synchrotron emission near the central black hole (BH). Due to a lack of angular resolution in existing observational facilities, such a study of the DM-induced signal in the inner part of M87 has not been performed yet—nor has it been done in similar objects. However, this is now possible with the advent of the Event Horizon Telescope (EHT).

Heavy DM particles annihilating into Standard Model particles near the central BH are expected to produce synchrotron emission in the frequency range that is currently being probed by the EHT. Here, we show that the synchrotron halo induced by DM is bright enough to be resolved by the EHT, if there is a DM spike. Moreover, this additional radiation enhances the photon ring around the BH shadow, thus making it a prominent feature in the EHT data and a new probe of the DM properties.

In Sec. II, we provide a description of the EHT, then we present our DM model in Sec. III and the EHT data we used in Sec. IV. Our results can be found in Sec. V, and we conclude in Sec. VI.

II. THE EVENT HORIZON TELESCOPE

A. General features

The EHT is a global network of millimeter and submillimeter facilities that employs very long baseline interferometry (VLBI) to create an effective Earth-scale high angular resolution telescope [2, 3]. The purpose of this array is to test general relativity and shed light on physical processes tak-

* lacroix@iap.fr

ing place in the vicinity of SMBHs at the centers of galaxies. To date, EHT data for M87 has been reported for a 3-station array comprised of the Submillimeter Telescope (SMT) in Arizona, the Combined Array for Research in Millimeter-wave Astronomy (CARMA) in California, and a network of three facilities in Hawaii: the James Clerk Maxwell Telescope (JCMT), the Submillimeter Array (SMA), and the Caltech Submillimeter Observatory (CSO). This configuration has already achieved an impressive angular resolution of order 40 μas at 230 GHz. Presently, the Atacama Large Millimeter/submillimeter Array (ALMA) in Chile, the Large Millimeter Telescope (LMT) in Mexico, the Institut de Radioastronomie Millimétrique (IRAM) 30m, the Plateau de Bure interferometer, and the South Pole Telescope (SPT)[1] will be added to the EHT. Longer term, the Greenland Telescope will join the array. Combined, the EHT will directly access angular scales as small as 26 μas at 230 GHz and 17 μas at 345 GHz.

The angular scale of the Schwarzschild radius of the SMBH at the center of M87 is about 8 μas.[2] The strong gravitational lensing near the black hole (BH) magnifies this by a factor of as much as 2.5, only weakly dependent of BH spin, making M87 a primary target for the EHT [3].

B. Imaging the shadow of a black hole

Characteristic in all images of optically thin emission surrounding BHs is a "shadow"—a dark central region surrounded by a brightened ring, the so-called "photon ring". This is a direct consequence of the strong gravitational lensing near the photon orbit, and is directly related to the projected image of the photon orbit at infinity. The shadow interior is the locus of null geodesics that intersect the horizon, and thus does not contain emission from behind the BH. The bright ring is in general sharply defined due to the instability of the photon orbit and a consequence of the pileup of higher-order images of the surrounding emission. For a Schwarzschild BH the radius of this shadow is $r_{\rm shadow} = 3\sqrt{3}/2R_{\rm S} \approx 2.6R_{\rm S}$ [7, 8]. For Kerr BHs, this radius ranges from $2.25R_{\rm S}$ to $2.6R_{\rm S}$, deviating substantially only at large values of the dimensionless spin parameter and viewed from near the equitorial plane, i.e., $a \gtrsim 0.9$ and $\theta \gtrsim 60^\circ$ [9].

The generic appearance of the shadow, its weak dependence on BH spin, and fundamentally general relativistic origin make it a prime feature in EHT science. Also imprinted on EHT images will be the high-energy astrophysics of the near-horizon region; the physics of BH accretion and relativistic jet formation. Horizon-scale features have already been observed in early EHT observations of Sagittarius A* (Sgr A*) [10–12] and M87 [13, 14], demonstrating that such structure exists. Here, we assess the observability of the shadow of the SMBH at the center of M87 in the electromagnetic signal from DM annihilation, and the limits that may be placed on DM properties given such a scenario.

[1] Note that M87 cannot be seen by the SPT.

[2] The mass of the central BH is $M_{\rm BH} = (6.4 \pm 0.5) \times 10^9 M_\odot$ [4], the corresponding Schwarzschild radius is $R_{\rm S} = 6 \times 10^{-4}$ pc and the distance of M87 is $d_{\rm M87} \approx 16$ Mpc [5]. Throughout we adopt the higher stellar dynamical mass for M87; using the $(3.5 \pm 0.8) \times 10^9 M_\odot$ value found by gas dynamical studies [6] would reduce the angular scales by roughly a factor of two througout.

III. PROBING A DARK MATTER SPIKE AT THE CENTER OF M87 WITH THE EVENT HORIZON TELESCOPE

In the context of the observational opportunities offered by the EHT, we now discuss the potential of this instrument in terms of DM searches. In particular, we study the observability of a DM spike at the center of M87, since such a sharply peaked morphological feature is expected to yield strong annihilation signals. At the frequencies of interest for the EHT, typically a few hundred GHz, the main DM signature comes from synchrotron radiation. Therefore, in order to assess the ability of the EHT to probe the inner part of the DM profile of M87, we need to compute the synchrotron emission of electrons and positrons produced in DM annihilations in the inner region. We make the following assumptions:

- The presence of a SMBH at the center is likely to lead to fairly strong magnetic fields, typically around 10–10^2 G [15]. As a result of such strong magnetic fields, synchrotron radiation and advection towards the central BH are the dominant physical processes by which DM-induced electrons and positrons lose or gain energy [16, 17], whereas inverse Compton scattering and bremsstrahlung are negligible. Additionally, the timescales associated with synchrotron radiation and advection are much shorter than that of spatial diffusion, so we disregard the latter in the following. Note that even larger magnetic fields—up to $\sim 10^3$ G—would arise if the equipartition scenario proposed in Ref. [18] for the center of the Milky Way were realized in M87. Therefore, to account for the uncertainty on the central magnetic field strength, we consider values in the range 10–10^3 G.

- We also disregard two processes that can reduce the synchrotron intensity. On the one hand, the synchrotron self-Compton effect, which would lead to additional energy losses for electrons and positrons, is only relevant for magnetic fields significantly smaller than 0.1 G [16]. For larger magnetic fields, such as the ones we consider here, synchrotron self-Compton losses are negligible with respect to synchrotron losses. On the other hand, synchrotron self-absorption is only relevant below $\sim$ 10 GHz [16, 17], so it can be neglected for the EHT frequency of 230 GHz.

- We assume the presence of a spike in the DM profile, formed through adiabatic growth of a SMBH [19] at the center of a DM halo with power-law density profile. The existence of such a strong enhancement of the DM density—corresponding to $\rho(r) \propto r^{-\gamma_{\rm sp}}$ with typically

$\gamma_{\rm sp} = 7/3$—is debated. It can actually be weakened by various dynamical processes such as mergers [20] (although the resolution of numerical simulations used to reach that conclusion is not sufficient to set strong constraints on the profile on sub-pc scales), if the BH did not grow exactly at the center of the DM halo [21, 22], or if the BH growth cannot be considered adiabatic [22]. Moreover, dynamical heating in the central stellar core would also soften a spike. However, an adiabatic spike is more likely to have survived in a dynamically young galaxy such as M87, in which stellar heating is essentially negligible, as discussed in Refs. [1, 23]. Furthermore, other dynamical processes can have the opposite effect of making the survival of a spike more likely; for instance enhanced accretion of DM to counteract the depopulation of chaotic orbits in triaxial halos [24]. Therefore in the following, we assume that an adiabatic spike effectively formed at early times at the center of M87 and has survived until today.

A. Electron propagation in the presence of advection

To derive the intensity of DM-induced synchrotron radiation, we first need to compute the electron and positron spectra from the DM annihilation rate. This is done by solving the propagation equation of DM-induced electrons and positrons which, in the presence of synchrotron radiation and advection, and assuming a steady state reads (see e.g. Refs. [16, 17]):

$$v\frac{\partial f_i}{\partial r} - \frac{1}{3r^2}\frac{\partial}{\partial r}\left(r^2 v\right) p\frac{\partial f_i}{\partial p} + \frac{1}{p^2}\frac{\partial}{\partial p}\left(p^2 \dot{p} f_i\right) = Q_i, \quad (1)$$

where $f_i(r,p)$ is the distribution function of electrons and positrons in momentum space, at radius r and momentum p, for annihilation channel i. The first, second and third terms correspond to the advection current, the energy gain of electrons due to the adiabatic compression, and the loss term due to radiative losses, respectively. $v(r) = -c\,(r/R_{\rm S})^{-1/2}$ is the radial infall velocity of electrons and positrons onto the BH in the accretion flow, where $R_{\rm S}$ is the Schwarzschild radius. The minus sign in the expression of the inflow velocity accounts for the direction of the flow, oriented towards the BH.

The source function $Q_i(r,p)$ is the DM annihilation rate in momentum space for channel i, related to the annihilation rate $q_i(r,E)$ in energy space via

$$Q_i(r,p) = \frac{c}{4\pi p^2} q_i(r,E) \quad (2)$$

in the ultra-relativistic (UR) regime where $E = pc$. The UR approximation can be safely used for electrons and positrons for the energy range relevant for this study. The usual annihilation rate in energy space reads:

$$q_i(r,E) = \frac{\langle\sigma v\rangle_i}{\eta}\left(\frac{\rho(r)}{m_{\rm DM}}\right)^2 \frac{{\rm d}N_{{\rm e},i}}{{\rm d}E}(E), \quad (3)$$

where $\eta = 2$ for the case of self-annihilating DM that we consider here. The injection spectrum ${\rm d}N_{{\rm e},i}/{\rm d}E$ is taken from Ref. [25] and the associated website.

Since radiative losses are dominated by synchrotron losses, the total radiative loss term $\dot{p} = {\rm d}p/{\rm d}t$ reduces to the synchrotron loss term [26]

$$\dot{p}(r,p) = \dot{p}_{\rm syn}(r,p) = -\frac{2\sigma_{\rm T} B^2 p^2}{3\mu_0 (m_{\rm e} c)^2}. \quad (4)$$

We assume the intensity of the magnetic field to be homogeneous, i.e. $B \equiv B_0$, over the accretion region, which has a size $r_{\rm acc}$ corresponding to the sphere of influence of the BH [17], so typically ~ 60 pc (as discussed in Ref. [1]), which is also roughly the size of the spike.

The resolution of the propagation equation, Eq. (1), in the presence of synchrotron losses and advection, in the UR regime, and with the method of characteristics, yields the electron and positron spectrum in terms of the DM annihilation rate [16]

$$f_i(r,p) = \frac{1}{c}\left(\frac{r}{R_{\rm S}}\right)\int_r^{r_{\rm acc}} Q_i(R_{\rm inj}, p_{\rm inj})\left(\frac{R_{\rm inj}}{R_{\rm S}}\right)^{\frac{5}{2}}\left(\frac{p_{\rm inj}}{p}\right)^4 {\rm d}R_{\rm inj}, \quad (5)$$

where the injection momentum $p_{\rm inj} \equiv p_{\rm inj}(R_{\rm inj}; r, p)$ for a homogeneous magnetic field is given in Appendix B. From there, the electron and positron energy spectrum is given by:

$$\psi_i(r,E) = \frac{4\pi p^2}{c} f_i(r,p). \quad (6)$$

We then convolve ψ_i with the synchrotron power $P_{\rm syn}(\nu,E,r)$ to obtain the synchrotron emissivity:

$$j_{{\rm syn},i}(\nu,r) = 2\int_{m_{\rm e}}^{m_{\rm DM}} P_{\rm syn}(\nu,E,r)\psi_i(r,E)\,{\rm d}E. \quad (7)$$

B. Relevance of advection

Advection shapes the inner part of the intensity profile by displacing electrons and positrons towards the BH, thereby accelerating them. This effect is in competition with synchrotron losses. Therefore, depending on the magnetic field, electrons either lose their energy in place through synchrotron radiation, or are first advected towards the center. The dependence on the magnetic field of the size of the region where electrons are affected by advection is obtained by comparing the synchrotron loss term given in Eq. (4) with the momentum gain rate due to adiabatic compression,

$$\dot{p}_{\rm ad} = -\frac{1}{3r^2}\frac{\partial}{\partial r}\left(r^2 v(r)\right) p. \quad (8)$$

The shape of the emissivity profile is thus governed by advection for:

$$r \lesssim \left(\frac{3R_{\rm S}^{\frac{1}{2}}\mu_0 m_{\rm e}^2 c^4}{4\sigma_{\rm T} B_0^2 E_{\rm syn}}\right)^{\frac{2}{3}}, \quad (9)$$

where $E_{\rm syn} = \left(4\pi m_{\rm e}^3 c^4 \nu/(3eB_0)\right)^{1/2}$ is the peak synchrotron energy at the frequency ν of interest [26]. In terms of the

angular distance from the center $\theta \equiv r/d_{\rm M87}$—where $d_{\rm M87} \approx 16$ Mpc is the distance between Earth and the center of M87—this condition reads, for $\nu = 230$ GHz,

$$\theta \lesssim 7 \left(\frac{B_0}{10\,{\rm G}}\right)^{-1} \mu{\rm as}. \quad (10)$$

It is therefore essential to include the advection process for $B_0 \lesssim 10$ G, since in that regime it has a strong impact on the synchrotron intensity in the region of interest for the EHT. For $B_0 \gg 10$ G, advection is negligible since it would only dominate for radii smaller than the Schwarzschild radius of the BH.

C. Dark synchrotron intensity in a curved spacetime

The DM-induced synchrotron intensity for a flat spacetime is computed by integrating the emissivity over the line of sight. However, the actual spacetime accounting for the presence of the SMBH at the center is characterized by the Schwarzschild or Kerr metric respectively if the BH is static or rotating. In these realistic cases, the correct spatial morphology of the synchrotron intensity I_ν is obtained using a ray-tracing technique that accounts for the gravitational lensing effect due to the BH. In our case, this is achieved via the ray-tracing and radiative transfer scheme described in Refs. [27–29].

IV. DATA

Here we provide a brief overview of the EHT data used to constrain our models. Details regarding individual observing runs, data calibration, and the uncertainty estimates can be found in Refs. [13, 14], to which we direct interested readers.

The EHT, like all interferometers, directly constructs visibilities by cross-correlating observations at pairs of stations. These are directly proportional to the Fourier transform of the image at a spatial frequency proportional to the ratio of the projected baseline distance between the two stations to the observation wavelength. Throughout the night the rotation of the Earth results in a rotation of the projected baseline, changing both its orientation and length, thereby generating a moderate variation in the spatial frequencies probed by any particular pair of sites.

Importantly, like any interferometer the EHT acts as a "high-pass" filter, sensitive primarily to structures on angular scales that lie between $\lambda/u_{\rm short}$ and $\lambda/u_{\rm long}$, where $u_{\rm short}$ and $u_{\rm long}$ are the shortest and longest baselines in the array, respectively. Within the context of the published EHT data on M87 these angular scales are 75 μas to 450 μas, though the high signal-to-noise ratio of the data extends these by roughly a factor of two. Therefore, features that extend over more than a milliarcsecond are effectively invisible to the EHT.

Upon measuring a sufficient number of these visibilities an image can be produced via inverting the Fourier transform. In practice, this is performed via a number of sophisticated image-inversion techniques that impose additional requirements on the final image, e.g., positivity, smoothness, etc [30]. However, because the published EHT observations only sparsely sample the spatial-frequency plane (often called the "u-v" plane) we compare directly with the measured visibilities.

By construction the visibilities are complex valued, and therefore described by an amplitude and phase. However, in practice the amplitudes are known much better than the phases as a result of the typically large, and highly variable, atmospheric phase delays. This does not mean that phase information is completely unavailable; "closure phases" constructed from triplets of sites, equal to the sum of the phases over the closed triangle of baselines, are insensitive to site-specific phase errors. Therefore, the two data sets we employ consist of visibility amplitudes and closure phases obtained with the Hawaii-SMT-CARMA array, reported in Refs. [13, 14]. In all cases observations were taken at 230 GHz.

Altogether, 160 visibility amplitudes were constructed from data taken on April 5, 6, and 7, 2009, reported in Ref. [13], and March 21, 2012, reported in Ref. [14]. All nights showed visbility amplitudes consistent with a single source structure. Of these 54 visibilities were reported on the CARMA-SMT baseline, 83 on the Hawaii-CARMA baseline, and 23 on the Hawaii-SMT baseline. Note that in all of the reported measurements a 5% systematic calibration error has been added to the uncertainties in quadrature.

On the Hawaii-CARMA-SMT triangle, 17 closure phases were constructed from data taken on March 21, 2012 and reported in Ref. [14]. Where visibility amplitudes provide a measure of the "power" in an image at a given spatial scale, closure phases are particularly sensitive to asymmetry; e.g., a point-symmetric image has identically zero closure phases. These are consistent with a constant closure phase of 0°, with typical uncertainties of 10°.

V. RESULTS

Predicted images are shown in Fig. 1, corresponding to the synchrotron intensity at 230 GHz from DM. The upper panels correspond to a DM spike with $\gamma_{\rm sp} = 7/3$, whereas the maps in the lower panels are computed for the no-spike case, for which we consider a standard Navarro-Frenk-White (NFW) DM profile with power-law index $\gamma = 1$. We assume annihilation of 10 GeV DM particles into $b\bar{b}$,[3] and a magnetic field of 10 G, for a static BH (left panels) and a maximally rotating BH (right panels).

The photon ring, i.e. the bright ring of radius ~ 20 μas that surrounds the darker shadow of the BH, is clearly visible in the simulations for all DM models we consider, although in practice in the absence of a spike the signal is too weak to be

[3] We focus on the standard b quark channel for simplicity. Injection of electrons through a different channel would primarily result in a rescaling of the intensity at the frequency of interest, slightly changing the best fit cross-sections we derive.

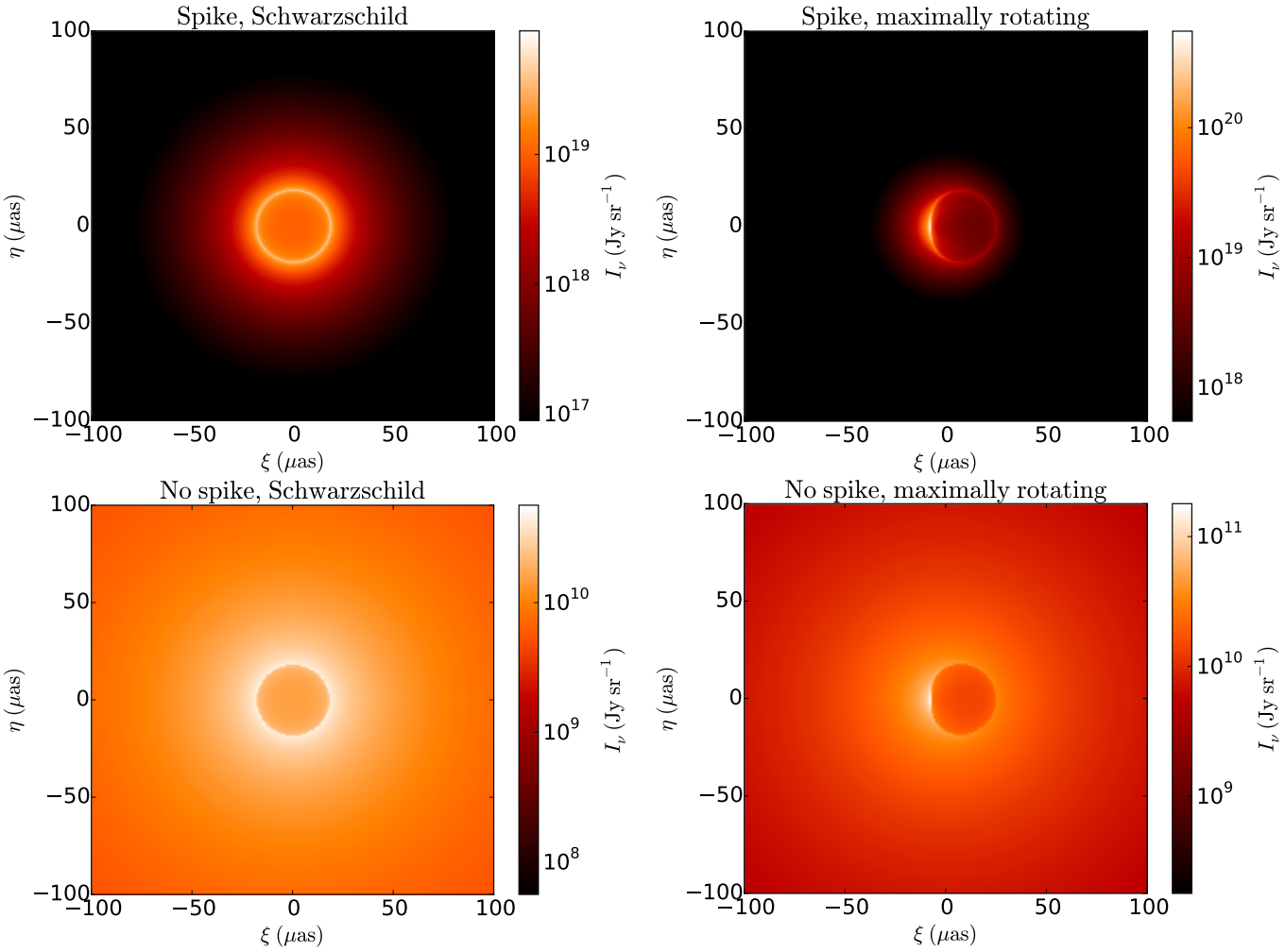

FIG. 1. Simulated maps of the synchrotron intensity at 230 GHz from a spike of 10 GeV DM annihilating into $b\bar{b}$, accounting for the strong gravitational lensing induced by the central BH, for a Schwarzschild BH (left panel) and a maximally rotating BH (right panel), in the presence (upper panels) and absence (lower panels) of a spike in the DM profile. Note that considering the wide range of intensities, we use different color scales, but with the same dynamic range spanning three orders of magnitude for comparison. The angular coordinates ξ and η correspond to the directions respectively perpendicular and parallel to the spin of the BH. For the spike cases, the slope of the DM spike is $\gamma_{\rm sp} = 7/3$, and the annihilation cross-sections correspond to the best fit to EHT observations (see text for details), namely 7.4×10^{-31} cm^3 s^{-1} for the Schwarzschild case and 3.1×10^{-31} cm^3 s^{-1} for the maximally rotating case. In the absence of a spike, the intensity is computed for the thermal s-wave cross-section of 3×10^{-26} cm^3 s^{-1}. For all the simulated maps the magnetic field is 10 G.

detectable with the EHT, as discussed in the following. The presence of a photon ring introduces small-scale structure into the signal, readily observable with the EHT on long baselines. For a static BH the shadow is exactly circular. For all but the most rapidly rotating BHs it is also very nearly circular [31, 32]. For a maximally rotating Kerr BH viewed from the equatorial plane the photon ring is flattened in the direction aligned with the BH spin.

At scales above 25 μas the DM spike-induced emission produces a diffuse synchrotron halo whose intensity falls with radius as a power law with index ≈ 3.5. This is generic, occuring independently of the BH spin and is present even when gravitational lensing is ignored. The extended nature of this component ensures that it is subdominant on Earth-sized baselines. In the absence of a spike, the profile is much flatter, and falls with radius as a power law with index ≈ 1. Fig. 1 also illustrates the fact that the intensity is significantly enhanced in the presence of a DM spike with respect to the no-spike case. To better stress this enhancement, we show the maps for the spike case computed for very small annihilation cross-sections of a few 10^{-31} cm^3 s^{-1}—corresponding to the best fits to the EHT data, as discussed below—, while in the absence of a spike we use the thermal s-wave cross-section of 3×10^{-26} cm^3 s^{-1}.

Shown in the blue solid line in Fig. 2 is the visibility amplitude at 230 GHz as a function of baseline length for the current EHT triangle, for the simulated DM-induced synchrotron signal, computed with a cross-section that gives the best fit to the EHT measurements from Refs. [13, 14]. The left panel corresponds to the Schwarzschild case and the right panel to the

maximally rotating case. The DM-induced visibility amplitudes shown in Fig. 2 correspond to the intensity maps shown in Fig. 1. Note that no additional astrophysical component has been included in these.

A standard NFW cusp actually results in visibility amplitudes that are about eight orders of magnitude lower than the EHT data. Note that these no-spike visibility amplitudes are not shown in Fig. 2 for clarity. Therefore, the EHT is only sensitive to spiky profiles, which makes it a dedicated probe of such sharply peaked DM distributions.[4]

As shown in Fig. 2, a spike of annihilating DM gives a good fit to the EHT measurements of the visibility amplitudes, with best fit cross-sections and reduced chi-squared—$\chi^2_{\rm red} = \chi^2/{\rm d.o.f.}$, with a number of degrees of freedom (d.o.f.) equal to 160 (data points) minus one (cross-section)—given in Tables I and II. While the fits appear by eye to be quite good, the reduced chi-squareds coupled with the large number of degrees of freedom result in a p-value < 0.002, implying that some structural component is missing in our model. This is not, in itself, surprising given the extraordinary simplicity of the DM spike model and our neglect of the contributions from the observed larger-scale radio emission associated with the jet.

The morphology of the predicted visibility amplitudes is only weakly sensitive to changes in the DM mass, the annihilation channel or the magnetic field, resulting primarily in different best-fit cross-sections. A small increase in the ratio of visibilities on long baselines to those on short baselines for larger magnetic fields arises from the higher intrinsic synchrotron peak coupled with the gravitational redshift, which increases the 230 GHz emission near the horizon.

The visibility amplitudes are more sensitive to the characteristics of the BH. Rotating BHs exhibit larger relative visibility amplitudes on long baselines than static BHs as a consequence of the bright emission from comparatively smaller radii. As a result, the quality of the fit is much better for a Schwarzschild BH.

The closure phases for the DM-spike-induced signal are shown in Fig. 3, for the Schwarzschild case (solid line) and the maximally rotating case (dashed line). The symmetry of the simulated signal is insensitive to the various parameters so we do not need to specify them here. As expected, the closure phase is identically zero for a Schwarzschild BH, while it is slightly larger than zero for the maximally rotating case. In both cases, closure phases for the DM-induced emission are consistent with the low closure phases observed.

Small closure phases are also typical of astrophysical models on the Hawaii-CARMA-SMT triangle [14]. This is because of the near degenerate nature of the projected baseline triangle due to the comparatively short CARMA-SMT baseline; closure phases on trivial triangles (in which one baseline has zero length) vanish identically. However, the inclusion of a number of additional sites in the near future will result in many additional, open triangles for which the closure phases are likely to differ substantially from zero [14]. These will be instrumental to discriminating both between astrophysical and DM-dominated models.

[4] Moreover, the intensity profile for the no-spike case is much flatter than for a spiky profile, leading to a larger ratio of flux on long to short baselines, with no significant contribution on long baselines.

VI. CONCLUSION

In this paper, we have demonstrated the potential of the EHT for DM searches. We have presented the first model of the DM-induced synchrotron emission in the close vicinity of a SMBH accounting for strong gravitational lensing effects. Our conclusions are the following.

- The synchrotron emission from DM spikes should be readily visible in EHT images of M87 if present. This remains true even for very small values of the annihilation cross-section. The resulting emission follows the structure of the DM spike, resulting in a synchrotron halo extending from horizon scales to roughly 100 μas.
- Within the spike emission, the silhouette of the BH is clearly visible on small scales for all spins and models we considered. This imparts small-scale structure on the image on scales of 50 μas, and contributes substantially to the visibilities on long baselines.
- DM spike emission provides an adequate fit to the existing horizon-scale structural constraints from the EHT. This necessarily ignores astrophysical contributions associated with the jet launching region. Such an additional astrophysical component is strongly motivated by the existence of extended emission at wavelengths of 3 mm and longer. Even within the 1.3 mm data, the fit quality suggests that the simple spike structures we present here are incomplete.
- Nevertheless, the limits on M87's flux and small-scale structure place corresponding constraints on the putative DM annihilation cross-sections. For a 10 GeV DM candidate this cross-section must be less than a few 10^{-31} cm^3 s^{-1}, close to the characteristic cross-sections for p-wave-suppressed annihilation. The introduction of additional astrophysical components would decrease this limit further.
- EHT observations in the near future will include a number of additional stations, enabling the reconstruction of M87's image with substantially higher fidelity. As a result, the limits on the existence of DM spikes and the properties of DM candidates will similarly improve. Thus, the EHT opens a new, powerful path to probing the structure and features of DM in the centers of galaxies.

ACKNOWLEDGMENTS

This work has been supported by UPMC, CNRS and STFC. This research has also received support at IAP from the ERC

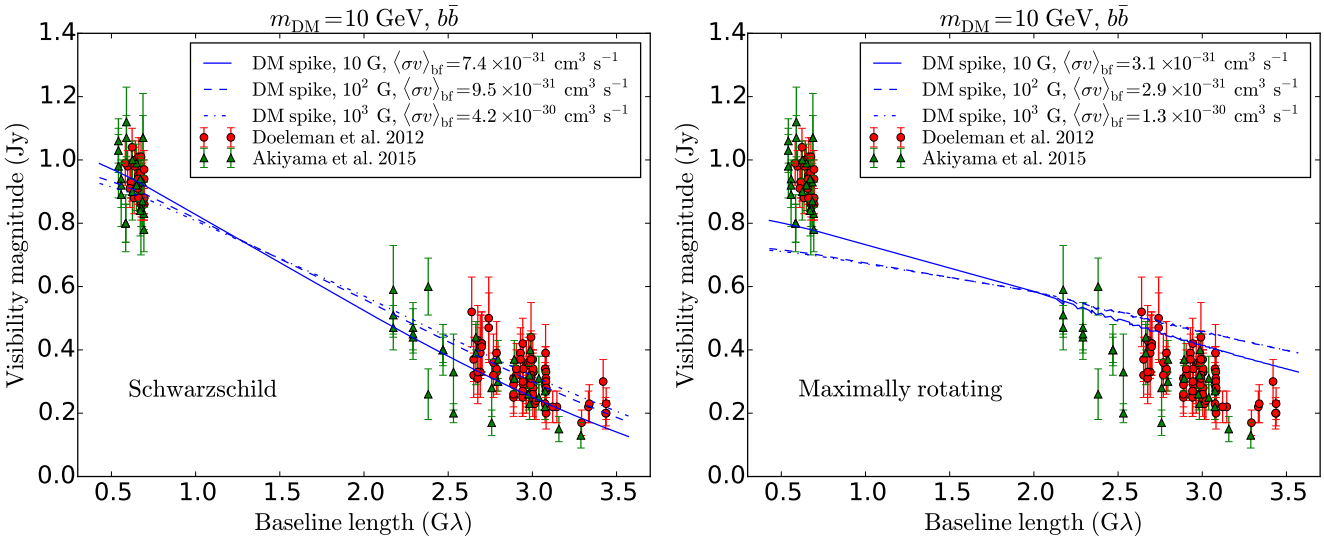
$m_{\rm DM}$=10 GeV, $b\bar{b}$
DM spike, 10 G, $\langle\sigma v\rangle_{\rm bf}$=7.4 ×10^{-31} cm^3 s^{-1}
DM spike, 10^2 G, $\langle\sigma v\rangle_{\rm bf}$=9.5 ×10^{-31} cm^3 s^{-1}
DM spike, 10^3 G, $\langle\sigma v\rangle_{\rm bf}$=4.2 ×10^{-30} cm^3 s^{-1}
Doeleman et al. 2012
Akiyama et al. 2015
Schwarzschild
Visibility magnitude (Jy)
Baseline length (Gλ)
$m_{\rm DM}$=10 GeV, $b\bar{b}$
DM spike, 10 G, $\langle\sigma v\rangle_{\rm bf}$=3.1 ×10^{-31} cm^3 s^{-1}
DM spike, 10^2 G, $\langle\sigma v\rangle_{\rm bf}$=2.9 ×10^{-31} cm^3 s^{-1}
DM spike, 10^3 G, $\langle\sigma v\rangle_{\rm bf}$=1.3 ×10^{-30} cm^3 s^{-1}
Doeleman et al. 2012
Akiyama et al. 2015
Maximally rotating
Visibility magnitude (Jy)
Baseline length (Gλ)

FIG. 2. Visibility amplitude at 230 GHz as a function of baseline length. The blue solid line represents the synchrotron emission from a spike of 10 GeV DM annihilating into $b\bar{b}$, with $B = 10$ G (solid), $B = 10^2$ G (dashed), and $B = 10^3$ G (dot-dashed), for a Schwarzschild BH (left panel) and a maximally rotating BH (right panel). The annihilation cross-sections correspond to the best fit to the EHT data from Refs. [13, 14], given in Tables I and II for the Schwarzschild and maximally rotating cases respectively.

TABLE I. Best fit annihilation cross-section and reduced chi-squared $\chi^2_{\rm red} = \chi^2/{\rm d.o.f.}$ for various DM masses and magnetic field strengths, for the Schwarzschild case. Values of the reduced chi-squared are given for illustration.

	$m_{\rm DM} = 10$ GeV	$m_{\rm DM} = 10^2$ GeV	$m_{\rm DM} = 10^3$ GeV
$B = 10$ G	$\langle\sigma v\rangle_{\rm bf} = 7.4\times10^{-31}$ cm^3 s^{-1}, $\chi^2_{\rm red} = 1.4$	$\langle\sigma v\rangle_{\rm bf} = 2.8\times10^{-29}$ cm^3 s^{-1}, $\chi^2_{\rm red} = 1.4$	$\langle\sigma v\rangle_{\rm bf} = 1.2\times10^{-27}$ cm^3 s^{-1}, $\chi^2_{\rm red} = 1.4$
$B = 10^2$ G	$\langle\sigma v\rangle_{\rm bf} = 9.5\times10^{-31}$ cm^3 s^{-1}, $\chi^2_{\rm red} = 1.5$	$\langle\sigma v\rangle_{\rm bf} = 4.4\times10^{-29}$ cm^3 s^{-1}, $\chi^2_{\rm red} = 1.5$	$\langle\sigma v\rangle_{\rm bf} = 1.8\times10^{-27}$ cm^3 s^{-1}, $\chi^2_{\rm red} = 1.5$
$B = 10^3$ G	$\langle\sigma v\rangle_{\rm bf} = 4.2\times10^{-30}$ cm^3 s^{-1}, $\chi^2_{\rm red} = 1.8$	$\langle\sigma v\rangle_{\rm bf} = 1.8\times10^{-28}$ cm^3 s^{-1}, $\chi^2_{\rm red} = 1.8$	$\langle\sigma v\rangle_{\rm bf} = 8.1\times10^{-27}$ cm^3 s^{-1}, $\chi^2_{\rm red} = 1.7$

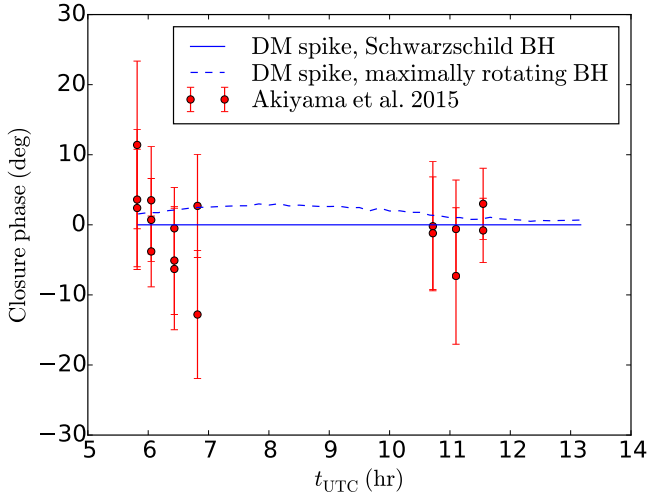

FIG. 3. Closure phase as a function of universal time, for a Schwarzschild BH (solid) and a maximally rotating BH (dashed), for the current VLBI triangle between Arizona, California and Hawaii.

Project No. 267117 (DARK) hosted by UPMC, and has been carried out in the ILP LABEX (ANR-10-LABX-63) and supported by French state funds managed by the ANR, within the Investissements d'Avenir programme (ANR-11-IDEX-0004-02). A.E.B. and M.K. receive financial support from the Perimeter Institute for Theoretical Physics and the Natural Sciences and Engineering Research Council of Canada through a Discovery Grant. Research at Perimeter Institute is supported by the Government of Canada through Industry Canada and by the Province of Ontario through the Ministry of Research and Innovation. We acknowledge support by the Canadian Institute for Advanced Research for the participation of A.E.B. and J.S. at the annual meetings of the CIFAR cosmology program where this project was initiated.

Appendix A: Normalization of the DM profile

Here we describe how we normalize the profile corresponding to a DM spike growing adiabatically from an initial power-

TABLE II. Best fit annihilation cross-section and reduced chi-squared $\chi^2_{\rm red} = \chi^2/{\rm d.o.f.}$ for various DM masses and magnetic field strengths, for the maximally rotating case. Values of the reduced chi-squared are given for illustration.

	$m_{\rm DM} = 10$ GeV	$m_{\rm DM} = 10^2$ GeV	$m_{\rm DM} = 10^3$ GeV
$B = 10$ G	$\langle\sigma v\rangle_{\rm bf} = 3.1\times10^{-31}$ cm^3 s^{-1}, $\chi^2_{\rm red} = 6.5$	$\langle\sigma v\rangle_{\rm bf} = 1.2\times10^{-29}$ cm^3 s^{-1}, $\chi^2_{\rm red} = 6.0$	$\langle\sigma v\rangle_{\rm bf} = 5.2\times10^{-28}$ cm^3 s^{-1}, $\chi^2_{\rm red} = 5.8$
$B = 10^2$ G	$\langle\sigma v\rangle_{\rm bf} = 2.9\times10^{-31}$ cm^3 s^{-1}, $\chi^2_{\rm red} = 11$	$\langle\sigma v\rangle_{\rm bf} = 1.3\times10^{-29}$ cm^3 s^{-1}, $\chi^2_{\rm red} = 11$	$\langle\sigma v\rangle_{\rm bf} = 5.6\times10^{-28}$ cm^3 s^{-1}, $\chi^2_{\rm red} = 11$
$B = 10^3$ G	$\langle\sigma v\rangle_{\rm bf} = 1.3\times10^{-30}$ cm^3 s^{-1}, $\chi^2_{\rm red} = 12$	$\langle\sigma v\rangle_{\rm bf} = 5.6\times10^{-29}$ cm^3 s^{-1}, $\chi^2_{\rm red} = 12$	$\langle\sigma v\rangle_{\rm bf} = 2.5\times10^{-27}$ cm^3 s^{-1}, $\chi^2_{\rm red} = 12$

law profile $\rho_0\,(r/r_0)^{-\gamma}$ [19] at the center of the M87 galaxy:

$$\rho(r) = \begin{cases} 0 & r < R_{\rm S} \\ \dfrac{\rho_{\rm sp}(r)\rho_{\rm sat}}{\rho_{\rm sp}(r)+\rho_{\rm sat}} & R_{\rm S} \le r < R_{\rm sp} \\ \rho_0 \left(\dfrac{r}{r_0}\right)^{-\gamma}\left(1+\dfrac{r}{r_0}\right)^{-2} & r \ge R_{\rm sp}, \end{cases} \tag{A1}$$

where the saturation density determined by DM annihilations reads

$$\rho_{\rm sat} = \frac{m_{\rm DM}}{\langle\sigma v\rangle\, t_{\rm BH}}, \tag{A2}$$

with $m_{\rm DM}$ and $\langle\sigma v\rangle$ respectively the mass and annihilation cross-section of the DM particle, and we take $t_{\rm BH} = 10^8$ yr for the age of the BH. The spike profile reads

$$\rho_{\rm sp}(r) = \rho_{\rm R}\left(\frac{R_{\rm sp}}{r}\right)^{\gamma_{\rm sp}}, \tag{A3}$$

where $\rho_{\rm R} = \rho_0\left(R_{\rm sp}/r_0\right)^{-\gamma}$, $R_{\rm sp} = \alpha_\gamma r_0\left(M_{\rm BH}/(\rho_0 r_0^3)\right)^{\frac{1}{3-\gamma}}$ and $\gamma_{\rm sp} = (9-2\gamma)/(4-\gamma)$. We use $M_{\rm BH} = 6.4\times10^9 M_\odot$ for the mass of the BH [4], the corresponding Schwarzschild radius is $R_{\rm S} = 6\times10^{-4}$ pc, and we take $\alpha_\gamma = 0.1$. We fix $r_0 = 20$ kpc for the halo (as for the Milky Way), and we must then determine the normalization ρ_0.

We choose ρ_0 in such a way that the profile is compatible with both the total mass of the galaxy and the mass enclosed within the radius of influence of the BH, of order $10^5 R_{\rm S}$. We thus follow the procedure described in Ref. [33]: the DM mass within the region that is relevant for the determination of the BH mass, typically within $R_0 = 10^5 R_{\rm S}$, must be smaller than the uncertainty on the BH mass $\Delta M_{\rm BH}$. ρ_0 is thus obtained by solving the following equation:

$$\int_{R_{\rm S}}^{10^5 R_{\rm S}} 4\pi r^2 \rho(r)\,{\rm d}r = \Delta M_{\rm BH}, \tag{A4}$$

with $\Delta M_{\rm BH} = 5\times10^8\ M_\odot$. Considering the complex dependence of ρ on ρ_0, we use the fact that the mass is dominated by the contribution from $r \gg R_{\rm S}$, i.e., typically $r > R_{\rm min} = O(100 R_{\rm S})$. In this regime we have $\rho \sim \rho_{\rm sp}(r)$. We can also factorize the dependence on ρ_0 in $\rho_{\rm sp}$, $\rho_{\rm sp}(r) = g_\gamma(r)\rho_0^{\frac{1}{4-\gamma}}\left(R'_{\rm sp}/r_0\right)^{-\gamma}\left(R'_{\rm sp}/r\right)^{\gamma_{\rm sp}}$, with $R'_{\rm sp} = \alpha_\gamma r_0\left(M_{\rm BH}/r_0^3\right)^{\frac{1}{3-\gamma}}$, and we finally obtain

$$\rho_0 = \left(\frac{\left(3-\gamma_{\rm sp}\right)\Delta M_{\rm BH}}{4\pi R_{\rm sp}^{\prime\gamma_{\rm sp}-\gamma} r_0^\gamma\left(R_0^{3-\gamma_{\rm sp}} - R_{\rm min}^{3-\gamma_{\rm sp}}\right)}\right)^{4-\gamma}. \tag{A5}$$

We take $\gamma = 1$, which corresponds to the NFW profile. The corresponding spike has a power-law index of $\gamma_{\rm sp} = 7/3$. Numerically, we get $\rho_0 \approx 2.5$ GeV cm^{-3} for $\gamma = 1$. Finally, the total mass within 50 kpc is $\sim 4\times10^{12}\ M_\odot$, compatible with the value derived from observations, $6\times10^{12}\ M_\odot$ [34].

In practice, the saturation radius $r_{\rm sat}$—for which $\rho_{\rm sat} = \rho(r_{\rm sat})$—is smaller than the Schwarzschild radius of the BH for all values of the DM mass and annihilation cross-section of interest here, so that the DM profile reads more simply

$$\rho(r) = \begin{cases} 0 & r < R_{\rm S} \\ \rho_{\rm sp}(r) & R_{\rm S} \le r < R_{\rm sp} \\ \rho_0 \left(\dfrac{r}{r_0}\right)^{-\gamma}\left(1+\dfrac{r}{r_0}\right)^{-2} & r \ge R_{\rm sp}. \end{cases} \tag{A6}$$

Note that one usually assumes that the DM profile vanishes below $4R_{\rm S}$ (or $2R_{\rm S}$ from the full relativistic calculation for a static BH [35]) due to DM particles captured by the BH. Here, for simplicity, to study the potential of the EHT for probing very steep power-law density profiles, we consider a DM spike that goes all the way down to the horizon of the BH, i.e. $R_{\rm S}$ for a Schwarzschild BH and $R_{\rm S}/2$ for a maximally rotating BH. However, this simplification has a negligible impact on our results.

Appendix B: Solving the cosmic-ray equation in the presence of an advection flow towards the central BH

The propagation equation of electrons and positrons in the presence of advection and synchrotron losses,

$$v\frac{\partial f}{\partial r} - \frac{1}{3r^2}\frac{\partial}{\partial r}\left(r^2 v\right) p\frac{\partial f}{\partial p} + \frac{1}{p^2}\frac{\partial}{\partial p}\left(p^2 \dot{p} f\right) = Q, \tag{B1}$$

can be rewritten as:

$$\frac{\partial f}{\partial r} + \frac{\dot{p}_{\rm ad} + \dot{p}_{\rm syn}}{v}\frac{\partial f}{\partial p} = -\frac{1}{v p^2}\frac{\partial}{\partial p}\left(p^2 \dot{p}_{\rm syn}\right) f + \frac{Q}{v}, \tag{B2}$$

where $\dot{p}_{\rm ad}$ is the momentum gain rate due to adiabatic compression in the advection process, and $v(r)$ the velocity field of the accretion flow. The associated characteristic curves are obtained by solving the following differential equation:

$$\frac{{\rm d}p}{{\rm d}r} = \frac{\dot{p}_{\rm ad} + \dot{p}_{\rm syn}}{v}. \tag{B3}$$

Generalizing the method of Ref. [16] to an arbitrary power-law profile for the magnetic field, $B(r) = B_0\,(r/R_{\rm S})^{-\alpha/2}$, solv-

ing Eq. (B3) with initial condition $p(R_{\rm inj}) = p_{\rm inj}$ leads to

$$p(r;R_{\rm inj},p_{\rm inj}) = p_{\rm inj} \times \left[\frac{k_0 R_{\rm S}^{\alpha-\frac{1}{2}}}{(\alpha-1)c} r^{\frac{3}{2}-\alpha} p_{\rm inj}\left(1-\left(\frac{r}{R_{\rm inj}}\right)^{\alpha-1}\right)+\left(\frac{r}{R_{\rm inj}}\right)^{\frac{1}{2}}\right]^{-1}, \quad \text{(B4)}$$

where

$$k_0 = \frac{2\sigma_{\rm T} B_0^2}{3\mu_0 (m_{\rm e} c)^2}. \quad \text{(B5)}$$

We consider the case $\alpha = 0$, corresponding to a homogeneous magnetic field.

The solution of the propagation equation in the ultrarelativistic regime is then given by

$$f(r,p) = \frac{1}{c}\left(\frac{r}{R_{\rm S}}\right)\int_r^{r_{\rm acc}} Q(R_{\rm inj},p_{\rm inj})\left(\frac{R_{\rm inj}}{R_{\rm S}}\right)^{\frac{5}{2}}\left(\frac{p_{\rm inj}}{p}\right)^4 {\rm d}R_{\rm inj}, \quad \text{(B6)}$$

where $p_{\rm inj} \equiv p_{\rm inj}(R_{\rm inj};r,p)$ is the injection momentum of an electron injected at $R_{\rm inj}$ ($\geq r$) and arriving at r with momentum p. Using Eq. (B4) and expressing $p_{\rm inj}$ as a function of p, we obtain, for $\alpha = 0$:

$$p_{\rm inj}(R_{\rm inj};r,p) = p\left[\frac{k_0 R_{\rm S}^{-\frac{1}{2}}}{c} R_{\rm inj}^{\frac{3}{2}} p\left(\frac{r}{R_{\rm inj}}-1\right)+\left(\frac{R_{\rm inj}}{r}\right)^{\frac{1}{2}}\right]^{-1}. \quad \text{(B7)}$$

Note that the denominator of $p_{\rm inj}$ can vanish and become negative, leading to nonphysical values of the injection momentum. This is related to the efficiency of the accretion flow and characterizes the region of the injection parameters $(R_{\rm inj}, p_{\rm inj})$ corresponding to a given arrival point (r,p). In practice, $p_{\rm inj}$ remains positive for $R_{\rm inj} < R_{\rm inj}^0$ where

$$R_{\rm inj}^0 = r + \frac{c}{k_0 p}\left(\frac{r}{R_{\rm S}}\right)^{-\frac{1}{2}}. \quad \text{(B8)}$$

We then use this value as an effective upper bound for the integral of Eq. (B6).

[1] T. Lacroix, C. Bœhm, and J. Silk, Phys. Rev. D **92**, 043510 (2015), arXiv:1505.00785.
[2] S. Doeleman, in *10th European VLBI Network Symposium and EVN Users Meeting: VLBI and the New Generation of Radio Arrays* (2010) p. 53.
[3] R.-S. Lu, A. E. Broderick, F. Baron, *et al.*, ApJ **788**, 120 (2014), arXiv:1404.7095 [astro-ph.IM].
[4] K. Gebhardt and J. Thomas, ApJ **700**, 1690 (2009), arXiv:0906.1492 [astro-ph.CO].
[5] S. Bird, W. E. Harris, J. P. Blakeslee, and C. Flynn, A&A **524**, A71 (2010), arXiv:1009.3202.
[6] J. L. Walsh, A. J. Barth, L. C. Ho, and M. Sarzi, ApJ **770**, 86 (2013), arXiv:1304.7273.
[7] J. M. Bardeen, in *Black Holes*, edited by C. Dewitt and B. S. Dewitt (1973) pp. 215–239.
[8] V. Bozza, General Relativity and Gravitation **42**, 2269 (2010), arXiv:0911.2187 [gr-qc].
[9] T. Johannsen and D. Psaltis, Advances in Space Research **47**, 528 (2011), arXiv:1008.3902 [astro-ph.HE].
[10] S. S. Doeleman, J. Weintroub, A. E. E. Rogers, *et al.*, Nature **455**, 78 (2008), arXiv:0809.2442.
[11] V. L. Fish, S. S. Doeleman, C. Beaudoin, *et al.*, ApJL **727**, L36 (2011), arXiv:1011.2472.
[12] V. L. Fish, M. D. Johnson, S. S. Doeleman, *et al.*, ApJ **820**, 90 (2016), arXiv:1602.05527.
[13] S. S. Doeleman, V. L. Fish, D. E. Schenck, *et al.*, Science **338**, 355 (2012), arXiv:1210.6132 [astro-ph.HE].
[14] K. Akiyama, R.-S. Lu, V. L. Fish, *et al.*, ApJ **807**, 150 (2015), arXiv:1505.03545 [astro-ph.HE].
[15] A. E. Broderick and A. Tchekhovskoy, ApJ **809**, 97 (2015), arXiv:1506.04754 [astro-ph.HE].
[16] R. Aloisio, P. Blasi, and A. V. Olinto, JCAP **5**, 007 (2004), arXiv:astro-ph/0402588.
[17] M. Regis and P. Ullio, Phys. Rev. D **78**, 043505 (2008), arXiv:0802.0234 [hep-ph].
[18] F. Melia, ApJL **387**, L25 (1992).
[19] P. Gondolo and J. Silk, Phys. Rev. Lett. **83**, 1719 (1999), arXiv:astro-ph/9906391.
[20] D. Merritt, M. Milosavljević, L. Verde, and R. Jimenez, Physical Review Letters **88**, 191301 (2002), arXiv:astro-ph/0201376.
[21] T. Nakano and J. Makino, ApJL **525**, L77 (1999), arXiv:astro-ph/9906131.
[22] P. Ullio, H. Zhao, and M. Kamionkowski, Phys. Rev. D **64**, 043504 (2001), arXiv:astro-ph/0101481.
[23] E. Vasiliev and M. Zelnikov, Phys. Rev. D **78**, 083506 (2008), arXiv:0803.0002.
[24] D. Merritt and M. Y. Poon, ApJ **606**, 788 (2004), arXiv:astro-ph/0302296.
[25] M. Cirelli, G. Corcella, A. Hektor, *et al.*, JCAP **3**, 051 (2011), arXiv:1012.4515 [hep-ph].
[26] M. S. Longair, *High Energy Astrophysics, by Malcolm S. Longair, Cambridge, UK: Cambridge University Press, 2011* (Cambridge University Press, 2011).
[27] A. E. Broderick, MNRAS **366**, L10 (2006), arXiv:astro-ph/0511515.
[28] A. E. Broderick and A. Loeb, ApJL **636**, L109 (2006a), arXiv:astro-ph/0508386.
[29] A. E. Broderick and A. Loeb, MNRAS **367**, 905 (2006b), arXiv:astro-ph/0509237.
[30] R.-S. Lu, A. E. Broderick, F. Baron, J. D. Monnier, V. L. Fish, S. S. Doeleman, and V. Pankratius, ApJ **788**, 120 (2014), arXiv:1404.7095 [astro-ph.IM].
[31] T. Johannsen and D. Psaltis, ApJ **718**, 446 (2010), arXiv:1005.1931 [astro-ph.HE].
[32] T. Johannsen, ApJ **777**, 170 (2013), arXiv:1501.02814 [astro-ph.HE].
[33] M. Gorchtein, S. Profumo, and L. Ubaldi, Phys. Rev. D **82**, 083514 (2010), arXiv:1008.2230 [astro-ph.HE].
[34] D. Merritt and B. Tremblay, Astron. J. **106**, 2229 (1993).
[35] L. Sadeghian, F. Ferrer, and C. M. Will, Phys. Rev. D **88**, 063522 (2013), arXiv:1305.2619 [astro-ph.GA].